Reversible Tuning of Luminescence and Magnetism in a Structurally Flexible Erbium-Anilato MOF

Noemi Monni,[a,b,d] José J. Baldoví,[b] Victor Garcia-Lopez,[b] Mariangela Oggianu,[a,d] Enzo Cadoni,[a] Francesco Quochi,*[c,d] Miguel Clemente-León,*[b] Maria Laura Mercuri*[a,d] and Eugenio Coronado[b]

[a]Dipartimento di Scienze Chimiche e Geologiche, Università degli Studi di Cagliari, Complesso Universitario di Monserrato, 09042 Monserrato, Italy.

[b]Instituto de Ciencia Molecular, Universitat de València, Catedrático José Beltrán 2, 46980 Paterna, Spain.

[c]Dipartimento di Fisica, Università degli Studi di Cagliari, Complesso Universitario di Monserrato, 09042 Monserrato, Italy

[d]INSTM, Via Giusti, 9 50121 Firenze, Italy

Supporting Informations

Index

1. Synthesis and Physical Measurements

GENERAL REMARKS. The Ln precursors, NaOH in pellets and the solvents used were purchased from Alfa Aesar and Exacta Optech and used without further purification. Synthesis of ligand H_2trz_2An was performed according with literature.[1] Elemental analyses (C, H, and N) were performed with a CE Instruments EA 1110 CHNS.

SYNTHESIS. *$[Er_2(trz_2An)_3(H_2O)_4]_n \cdot 10H_2O$ (**1a**) and $[Er_2(trz_2An)_3(H_2O)_4]_n \cdot 7H_2O$ (**1b**)*. A 5 mL Teflon vial with a mixture of $Er(NO_3)_3 \cdot 6H_2O$ (0.05 mmol; 22.2 mg), H_2trz_2An (0.05 mmol, 13.7 mg), NaOH (0.1 mmol, 4 mg) and water (5 mL) was heated at 130°C for 48 hours and then the vial was slowly cooled to room temperature. Two different types of crystals were obtained from the same batch, dark red-block crystals (**phase a**) and orange prismatic crystals (**phase b**), both of them were suitable for SC-XRD measurements. Their density's difference was exploited to separate them, using CH_2Cl_2/CH_2Br_2 solvent mixture in the ratio 0.925/0.975, for all further measurements. Elemental analysis of **1a** and **1b** is reported below in **Table 1**. Both single crystals and polycrystalline powder of **1a** were placed under vacuum in a vacuum line pump and then sealed in a glove box to obtain *$[Er_2(trz_2An)_3(H_2O)_2]_n \cdot 2H_2O$ (**1a_des**),* whereas the same attempt on **1b** produced no changes. Elemental analysis of **1a_des** is not shown since it turns to the structure of **1a** after two days in air (see below).

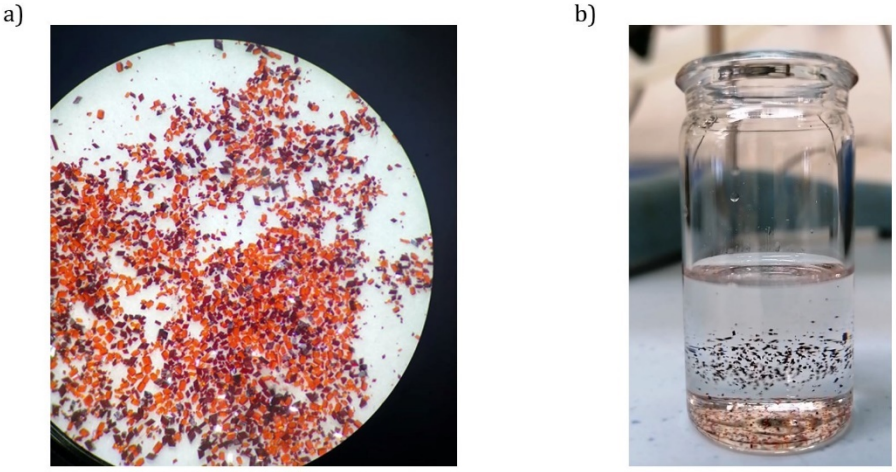

Figure S1. a) Optical microscope image of a mixture of crystals of phase **a** and **b**; b) crystals separations using the CH_2Cl_2/CH_2Br_2 solution mix.

Table S1. Elemental analysis for all the compounds **1a** and **1b**.

		Calculated			Found		
		%C	%H	%N	%C	%H	%N
1a	$C_{30}H_{40}N_{18}O_{26}Er_2$	25.68	2.87	17.97	25.37	2.81	17.86
1b	$C_{30}H_{34}N_{18}O_{23}Er_2$	26.71	2.54	18.69	26.70	2.24	18.57

PHYSICAL MEASUREMENTS.

A detailed description of **X-Ray Diffraction** experimental setup and additional data is provided in *paragraph 2*.

Thermogravimetric Analysis. Thermogravimetric analyses were performed in alumina crucibles with the instrument STA-6000 under nitrogen flux (40 mL/min), in the 25-800°C temperature range at 10°C/min.

Magnetic Measurements. Magnetic measurements were performed with Quantum Design MPMS-XL-5 SQUID and PPMS-9 magnetometers on powdered polycrystalline samples measured with eicosane to avoid preferential orientations. In the case of **1a**, it was necessary to protect the sample covering it with H_2O in a glass tube since the vacuum of the squid chamber caused desolvation and the formation of **1a_des**. Thus, magnetic measurements of **1a** in the absence of H_2O correspond to **1a_des**.

Theoretical Calculations. For the theoretical modelling of the magnetic properties, we have used the SIMPRE computational package,[2] introducing the crystallographic atomic coordinates and the experimental magnetic properties of the compounds as an input. In order to fit the experimental data, we have varied the two parameters (D_r and Z_i) of the REC model for each type of donor atom of the first coordination sphere.[3] A detailed explanation is provided in *paragraph 6*.

Photoluminescence Measurements. Photoluminescence (PL) experiments were performed with pulsed laser irradiance at 355 nm wavelength. Finely ground powders were compacted between quartz slides for measurements in standard conditions, or attached to the cold finger of a continuous-flow cryostat (Janis ST-500) for measurements under controlled atmosphere (air, vacuum, N_2), fed with liquid N_2 for low-temperature measurements under vacuum conditions at

77K. For time-resolved measurements of the ligand-centered emissions, samples were excited by optical parametric amplifier (Light Conversion TOPAS-C) emitting ~200-fs-long pulses at the repetition frequency of 1 kHz and detected by a Vis streak camera (Hamamatsu C1091) connected to a single-grating spectrometer (Princeton Instruments Acton SpectraPro2300i). For all other PL experiments, samples were pumped by a passively Q-switched powerchip laser (Teem Photonics PNV-M02510) delivering ~350 ps pulses, centered at 355 nm wavelength, at 1 kHz. The PL signals were analyzed by a single-grating spectrometer (Princeton Instruments Acton SpectraPro 2300i) and acquired by thermoelectrically cooled detectors, namely, (a) a Vis CCD camera (Andor NewtonEM) for ligand-centered emission spectra, (b) a NIR array detector (Andor iDus InGaAs 1.7mm) for NIR PL spectra, and (c) a photomultiplier (Hamamatsu H10330A-75) connected to a 1 GHz digital oscilloscope (Tektronix TDS 5104) for NIR PL decay transients.

2. X-Ray Diffraction

Single crystal X-Ray diffraction was performed on **1a** and **1b** crystals, which were mounted on a glass fiber using a viscous hydrocarbon oil to coat the single crystal and then transferred directly to the cold nitrogen stream for data collection. X ray data were collected at 120 K for both samples. Furthermore, a single crystal of **1a** was measured at 360 K (**1a_des** 360 K) and another one was measured at 120 K after being placed in vacuum under a vacuum line pump and were then opened in the glove box to be sealed and mounted on a glass fiber using a viscous hydrocarbon oil to coat the single crystal. Then, the sample was transferred to the cold nitrogen stream for data collection (**1a_des** vacuum). Measurements were performed on a Supernova diffractometer equipped with a graphite-monochromated Enhance (Mo) X-ray Source (λ = 0.710 73 Å). The program CrysAlisPro, Oxford Diffraction Ltd., was used for unit cell determinations and data reduction. Empirical absorption correction was performed using spherical harmonics, implemented in the SCALE3 ABSPACK scaling algorithm. The structures were solved with the ShelXT structure solution program[4] and refined with the SHELXL-2013 program,[5] using Olex2.[6] Non-hydrogen atoms were refined anisotropically, and hydrogen atoms were placed in calculated positions refined using idealized geometries (riding model) and assigned fixed isotropic displacement parameters. Single crystal diffraction data of **1a_des** are of very bad quality due to the loss of single crystallinity under vacuum or temperatures above 350 K but good enough to solve the structure. Dehydration caused structural damage of part of the crystal, which could be responsible of several A and B errors in the checkcif files. Crystallographic data of all the compounds are summarized in **Table S2.** Crystallographic data for the structures was deposited in the Cambridge Crystallographic Data Centre, deposition numbers CCDC 2130639-42. These data can be obtained

free of charge from The Cambridge Crystallographic Data Centre via www.ccdc.cam.ac.uk/data_request/cif.

Powder X-ray diffraction (PXRD) patterns were performed using a 0.7 mm glass capillary filled with polycrystalline samples of the compounds and mounted and aligned on an Empyrean PANalytical powder diffractometer, using Cu Kα radiation (λ = 1.541 77 Å). A total of three scans were collected for each compound at room temperature in the 2θ range of 5−40°. Polycrystalline samples of **1a** and **1b** were further placed under vacuum in a vacuum line pump and were then opened in the glove box to be sealed in the 0.7 mm glass capillary.

Table S2. Crystallographic data for compound **1a**, **1a_des** and **1b**.

	1a	**1a_des (360 K)**	**1a_des (vacuum)**	**1b**
Empirical formula	$C_{30}H_{28}N_{18}O_{25}Er_2$	$C_{30}H_{16}N_{18}O_{15}Er_2$	$C_{30}H_{14}N_{18}O_{18}Er_2$	$C_{30}H_{28}N_{18}O_{20}Er_2$
FW	1.375.22	1203.12	1249.12	1295.22
Crystal color	Dark Purple	Purple	Purple	Orange
Crystal size (mm^3)	0.24 × 0.15 × 0.07	0.19 × 0.18 × 0.11	0.29 × 0.24 × 0.12	0.24 × 0.15 × 0.13
Temperature (K)	120	360	120	120
Wavelength (Å)	(MoKa) λ = 0.71073	(MoKa) λ = 0.71073	(MoKa) λ = 0.71073	(MoKa) λ = 0.71073
Crystal system	triclinic	triclinic	triclinic	triclinic
Space group	*P-1*	*P-1*	*P-1*	*P-1*
a (Å)	8.9555 (7)	9.0051 (13)	9.013(3)	8.6201(3)
b (Å)	9.4191 (7)	9.3427 (17)	9.200(3)	10.4220 (4)
c (Å)	15.4553 (12)	12.533 (2)	12.495(3)	11.9887(4)
a (°)	75.154 (7)	93.979 (15)	94.90(2)	80.139(3)
b (°)	77.176 (7)	97.759 (14)	98.10(2)	79.145(3)
g (°)	67.936 (7)	115.991 (16)	115.67(3)	82.373(3)
V (Å³)	1156.33 (17)	929.3 (3)	912.1(5)	1036.52(7)
ρ_{calc} ($g.cm^{-3}$)	1.975	2.150	2.274	2.075
μ(MoKα) (mm^{-1})	3.712	4.584	4.681	4.126
2θ range (°)	5.59 to 55.74	6.078 to 52.78	6.15 to 56.152	6.584 to 56.08
Index ranges	$-11 \le h \le 11$, $-11 \le k \le 12$, $-17 \le l \le 20$	$-10 \le h \le 11$, $-11 \le k \le 11$, $-15 \le l \le 15$	$-11 \le h \le 11$, $-12 \le k \le 11$, $-15 \le l \le 16$	$-11 \le h \le 11$, $-13 \le k \le 12$, $-15 \le l \le 14$
Reflections collected	7799	9454	10668	14194
Independent reflections	4608 [R_{int} = 0.0362, R_{sigma} = 0.0667]	3640 [R_{int} = 0.1450, R_{sigma} = 0.1500]	3881 [R_{int} = 0.1745, R_{sigma} = 0.2099]	4366 [R_{int} = 0.0203, R_{sigma} = 0.0223]
Data/restraints/parameters	4608/0/339	3640/0/270	3881/2/272	4366/0/324
Goodness-of-fit on F2	1.046	1.111	1.090	1.055
Final R indexes [I>=2σ (I)]	R_1 = 0.0354, wR_2 = 0.0680	R_1=0.1222, wR_2=0.2922	R_1=0.1400,wR_2=0.2986	R_1=0.0155,wR_2=0.0370
Final R indexes [all data]	R_1 = 0.0414, wR_2 = 0.0735	R_1=0.1678, wR_2 = 0.3317	R_1=0.2072,wR_2=0.3613	R_1=0.0162,wR_2=0.0373
Largest diff. peak/hole/e $Å^{-3}$	1.21/-1.47	3.73/-3.05	4.79/-2.83	0.88/-0.93

Table S3. Bond lengths (Å) in **1a**.

Bond Lengths (Å)					
Er1	O3	2.319(3)	N1	C4	1.329(6)
Er1	O4[1]	2.416(3)	N1	C2	1.429(6)
Er1	O7	2.377(3)	C7	C8	1.385(7)
Er1	O5	2.377(3)	C7	C6	1.396(6)
Er1	O1	2.409(3)	C8	C6[1]	1.545(6)
Er1	O2[2]	2.426(3)	N7	C12	1.435(6)
Er1	O8	2.369(3)	N7	N8	1.377(5)
Er1	O6[3]	2.433(3)	N7	C14	1.323(6)
Er1	N3[4]	2.461(4)	N2	C5	1.313(6)
O3	C6	1.247(6)	N6	C9	1.337(6)
O4	C8	1.250(5)	N6	C10	1.342(7)
O5	C11	1.254(6)	C12	C13	1.397(7)
O1	C1	1.241(6)	C12	C11	1.395(7)
O2	C3	1.268(6)	N9	C14	1.314(6)
O6	C13	1.246(6)	N9	C15	1.356(7)
N3	C4	1.331(6)	N5	C10	1.320(7)
N3	C5	1.347(6)	N8	C15	1.318(6)
N4	C7	1.438(6)	C2	C1	1.404(6)
N4	N5	1.367(5)	C2	C3	1.386(7)
N4	C9	1.326(6)	C13	C11[3]	1.530(6)
N1	N2	1.369(6)	C1	C3[2]	1.532(6)

Table S4. Bond angles (°) in **1a**.

Bond Angles (°)							
O3	Er1	O4[1]	66.19(10)	C9	N4	C7	129.6(4)
O3	Er1	O7	87.90(11)	C9	N4	N5	108.9(4)
O3	Er1	O5	72.95(11)	N2	N1	C2	121.1(4)
O3	Er1	O1	69.95(11)	C4	N1	N2	110.1(4)
O3	Er1	O2[2]	135.11(11)	C4	N1	C2	128.8(4)
O3	Er1	O8	83.36(11)	C8	C7	N4	122.0(4)
O3	Er1	O6[3]	134.50(11)	C8	C7	C6	120.2(4)
O3	Er1	N3[4]	141.28(13)	C6	C7	N4	117.8(4)
O4[1]	Er1	O2[2]	137.35(11)	O4	C8	C7	125.8(4)
O4[1]	Er1	O6[3]	132.63(11)	O4	C8	C6[1]	114.5(4)
O4[1]	Er1	N3[4]	75.13(12)	C7	C8	C6[1]	119.7(4)
O7	Er1	O4[1]	68.06(12)	N8	N7	C12	122.0(4)
O7	Er1	O5	137.77(11)	C14	N7	C12	127.9(4)
O7	Er1	O1	69.60(11)	C14	N7	N8	110.1(4)
O7	Er1	O2[2]	75.70(12)	C5	N2	N1	101.9(4)
O7	Er1	O6[3]	135.81(12)	C9	N6	C10	101.2(4)
O7	Er1	N3[4]	79.16(12)	O3	C6	C7	125.2(4)
O5	Er1	O4[1]	130.45(11)	O3	C6	C8[1]	114.8(4)
O5	Er1	O1	68.53(12)	C7	C6	C8[1]	120.0(4)
O5	Er1	O2[2]	91.64(12)	C13	C12	N7	118.1(4)
O5	Er1	O6[3]	65.36(11)	C11	C12	N7	119.5(4)
O5	Er1	N3[4]	137.59(12)	C11	C12	C13	122.2(4)
O1	Er1	O4[1]	118.62(11)	C14	N9	C15	103.0(4)
O1	Er1	O2[2]	65.18(10)	N1	C4	N3	109.7(4)
O1	Er1	O6[3]	108.72(12)	C10	N5	N4	101.9(4)
O1	Er1	N3[4]	135.17(12)	C15	N8	N7	101.2(4)

O2[2]	Er1	O6[3]	65.14(12)	C1	C2	N1	117.7(4)
O2[2]	Er1	N3[4]	76.69(12)	C3	C2	N1	120.4(4)
O8	Er1	O4[1]	68.63(12)	C3	C2	C1	121.9(4)
O8	Er1	O7	135.63(13)	O6	C13	C12	125.3(4)
O8	Er1	O5	80.19(12)	O6	C13	C11[3]	115.4(4)
O8	Er1	O1	143.41(11)	C12	C13	C11[3]	119.3(4)
O8	Er1	O2[2]	136.39(11)	N2	C5	N3	115.3(5)
O8	Er1	O6[3]	72.65(12)	O5	C11	C12	126.5(4)
O8	Er1	N3[4]	81.06(13)	O5	C11	C13[3]	115.1(4)
O6[3]	Er1	N3[4]	72.83(12)	C12	C11	C13[3]	118.4(4)
C6	O3	Er1	124.0(3)	O1	C1	C2	125.1(4)
C8	O4	Er1[1]	120.4(3)	O1	C1	C3[2]	115.5(4)
C11	O5	Er1	119.5(3)	C2	C1	C3[2]	119.4(4)
C1	O1	Er1	122.4(3)	O2	C3	C2	126.5(4)
C3	O2	Er1[2]	120.6(3)	O2	C3	C1[2]	115.0(4)
C13	O6	Er1[3]	118.1(3)	C2	C3	C1[2]	118.6(4)
C4	N3	Er1[5]	127.4(3)	N9	C14	N7	110.5(4)
C4	N3	C5	103.0(4)	N4	C9	N6	111.6(5)
C5	N3	Er1[5]	128.7(3)	N8	C15	N9	115.2(4)
N5	N4	C7	121.5(4)	N5	C10	N6	116.3(4)

Table S5. Bond lengths (Å) in **1b**.

Bond lengths (Å)					
C1	C2	1.395(3)	C11	C13[3]	1.530(3)
C1	C3[1]	1.530(3)	C11	O5	1.256(3)
C1	O1	1.254(3)	C12	C13	1.407(3)
C2	C3	1.400(3)	C12	N7	1.425(3)
C2	N1	1.420(3)	C13	O6	1.241(3)

C3	O2	1.245(3)	C14	N8	1.315(3)
C4	N1	1.333(3)	C14	N9	1.357(3)
C4	N3	1.317(3)	C15	N7	1.331(3)
C5	N2	1.315(3)	C15	N9	1.322(3)
C5	N3	1.355(3)	Er1	N6[4]	2.5317(19)
C6	C7	1.397(3)	Er1	O1	2.3648(15)
C6	C8[2]	1.537(3)	Er1	O2[1]	2.5060(16)
C6	O3	1.256(3)	Er1	O3	2.3505(15)
C7	C8	1.403(3)	Er1	O4[2]	2.3928(15)
C7	N4	1.427(3)	Er1	O5	2.3336(15)
C8	O4	1.242(3)	Er1	O6[3]	2.4919(15)
C9	N4	1.332(3)	Er1	O7	2.3245(15)
C9	N6	1.320(3)	Er1	O8	2.3423(16)
C10	N5	1.310(3)	N1	N2	1.368(3)
C10	N6	1.356(3)	N4	N5	1.369(3)
C11	C12	1.393(3)	N7	N8	1.370(3)

Table S6. Bond angles (°) in **1b**.

Bond Angles (°)							
C2	C1	C3[1]	120.9(2)	O5	Er1	N6[4]	70.51(6)
O1	C1	C2	124.0(2)	O5	Er1	O1	137.48(5)
O1	C1	C3[1]	115.13(19)	O5	Er1	O2[1]	142.92(5)
C1	C2	C3	121.5(2)	O5	Er1	O3	135.83(5)
C1	C2	N1	116.9(2)	O5	Er1	O4[2]	91.72(5)
C3	C2	N1	121.6(2)	O5	Er1	O6[3]	65.68(5)
C2	C3	C1[1]	117.58(19)	O5	Er1	O8	77.04(6)
O2	C3	C1[1]	115.53(19)	O6[3]	Er1	N6[4]	117.29(6)
O2	C3	C2	126.9(2)	O6[3]	Er1	O2[1]	126.52(5)

N3	C4	N1	111.7(2)	O7	Er1	N6^{4}	142.02(6)
N2	C5	N3	115.8(2)	O7	Er1	O1	137.57(6)
C7	C6	C8^{2}	119.35(19)	O7	Er1	O2^{1}	73.46(5)
O3	C6	C7	124.4(2)	O7	Er1	O3	87.57(5)
O3	C6	C8^{2}	116.27(19)	O7	Er1	O4^{2}	136.38(5)
C6	C7	C8	122.5(2)	O7	Er1	O5	81.29(6)
C6	C7	N4	118.09(19)	O7	Er1	O6^{3}	69.99(5)
C8	C7	N4	119.44(19)	O7	Er1	O8	76.67(6)
C7	C8	C6^{2}	118.17(19)	O8	Er1	N6^{4}	72.67(6)
O4	C8	C6^{2}	116.60(19)	O8	Er1	O1	93.86(6)
O4	C8	C7	125.2(2)	O8	Er1	O2^{1}	71.09(5)
N6	C9	N4	110.48(19)	O8	Er1	O3	141.17(6)
N5	C10	N6	114.8(2)	O8	Er1	O4^{2}	143.62(5)
C12	C11	C13^{3}	119.83(19)	O8	Er1	O6^{3}	132.66(5)
O5	C11	C12	124.4(2)	C4	N1	C2	127.2(2)
O5	C11	C13^{3}	115.79(19)	C4	N1	N2	108.81(19)
C11	C12	C13	122.2(2)	N2	N1	C2	123.31(19)
C11	C12	N7	116.91(19)	C5	N2	N1	102.0(2)
C13	C12	N7	120.81(19)	C4	N3	C5	101.6(2)
C12	C13	C11^{3}	117.95(19)	C9	N4	C7	129.33(19)
O6	C13	C11^{3}	115.98(19)	C9	N4	N5	109.27(18)
O6	C13	C12	126.1(2)	N5	N4	C7	121.24(18)
N8	C14	N9	114.4(2)	C10	N5	N4	102.55(18)
N9	C15	N7	110.4(2)	C9	N6	C10	102.90(19)
O1	Er1	N6^{4}	67.15(6)	C9	N6	Er1^{5}	129.68(15)
O1	Er1	O2^{1}	64.42(5)	C10	N6	Er1^{5}	126.94(15)
O1	Er1	O4^{2}	71.19(5)	C15	N7	C12	129.08(19)
O1	Er1	O6^{3}	133.34(5)	C15	N7	N8	109.30(18)

O2[1]	Er1	N6[4]	115.65(6)	N8	N7	C12	119.53(18)
O3	Er1	N6[4]	130.40(6)	C14	N8	N7	102.70(18)
O3	Er1	O1	74.20(5)	C15	N9	C14	103.18(19)
O3	Er1	O2[1]	70.45(5)	C1	O1	Er1	125.02(14)
O3	Er1	O4[2]	67.91(5)	C3	O2	Er1[1]	119.87(14)
O3	Er1	O6[3]	70.33(5)	C6	O3	Er1	118.11(14)
O4[2]	Er1	N6[4]	70.96(6)	C8	O4	Er1[2]	117.28(14)
O4[2]	Er1	O2[1]	125.26(5)	C11	O5	Er1	123.67(14)
O4[2]	Er1	O6[3]	67.97(5)	C13	O6	Er1[3]	118.39(14)

Table S7. Bond lengths (Å) in **1a_des** (vacuum).

Bond lengths (Å)					
Er01	O002	2.264(17)	N00B	C00V	1.37(3)
Er01	O003	2.430(16)	N00D	C00N	1.28(3)
Er01	O004	2.388(14)	N00D	C00O	1.36(3)
Er01	O005	2.285(16)	N00E	N00L	1.36(3)
Er01	O006	2.264(17)	N00E	C00T	1.30(3)
Er01	O007[1]	2.418(17)	N00E	C00W	1.41(3)
Er01	O00A[2]	2.394(17)	N00G	C00O	1.32(3)
Er01	N00B[3]	2.47(2)	N00H	C00V	1.34(3)
O002	C00S	1.25(2)	C00I	C00R	1.42(3)
O003	C00K	1.22(3)	C00I	C00U	1.40(3)
O004	C00M	1.25(3)	C00J	C00M	1.36(3)
O005	C00U	1.26(2)	C00J	C00P	1.38(3)
O007	C00P	1.23(3)	C00K	C00S	1.60(3)
N008	C00F	1.37(3)	C00K	C00W[4]	1.45(3)
N008	N00H	1.33(3)	N00L	C00X	1.33(3)
N008	C00J	1.45(3)	C00M	C00P[1]	1.57(3)

N009	N00G	1.42(2)	N00Q	C00T	1.36(3)
N009	C00I	1.38(3)	N00Q	C00X	1.36(3)
N009	C00N	1.32(3)	C00R	C00U[2]	1.55(3)
O00A	C00R	1.24(3)	C00S	C00W	1.37(3)
N00B	C00F	1.35(3)			

Table S8. Bond angles (°) in **1a_des** (vacuum).

Bond Angles (°)							
O002	Er01	O003	66.3(5)	C00V	N00B	Er01[3]	131.5(15)
O002	Er01	O004	87.0(6)	C00N	N00D	C00O	102(2)
O002	Er01	O005	148.5(5)	N00L	N00E	C00W	121(2)
O002	Er01	O007[1]	76.8(6)	C00T	N00E	N00L	110(2)
O002	Er01	O00A[2]	81.7(6)	C00T	N00E	C00W	129(2)
O002	Er01	N00B[3]	141.3(6)	N00B	C00F	N008	107(2)
O003	Er01	N00B[3]	75.0(6)	C00O	N00G	N009	101.0(19)
O004	Er01	O003	66.3(5)	N008	N00H	C00V	103(2)
O004	Er01	O007[1]	64.2(5)	N009	C00I	C00R	118(2)
O004	Er01	O00A[2]	130.6(5)	N009	C00I	C00U	124(2)
O004	Er01	N00B[3]	78.3(5)	C00U	C00I	C00R	118(2)
O005	Er01	O003	144.5(6)	C00M	C00J	N008	118(2)
O005	Er01	O004	109.8(6)	C00M	C00J	C00P	124(2)
O005	Er01	O007[1]	86.8(6)	C00P	C00J	N008	118(2)
O005	Er01	O00A[2]	67.1(6)	O003	C00K	C00S	116.7(17)
O005	Er01	N00B[3]	69.8(6)	O003	C00K	C00W[4]	125(2)
O006	Er01	O002	85.5(6)	C00W[4]	C00K	C00S	118.0(19)
O006	Er01	O003	77.1(5)	C00X	N00L	N00E	101(2)
O006	Er01	O004	142.5(6)	O004	C00M	C00J	128(2)

O006	Er01	O005	95.1(6)	O004	C00M	C00P[1]	112.8(19)
O006	Er01	O007[1]	147.5(6)	C00J	C00M	C00P[1]	119(2)
O006	Er01	O00A[2]	84.5(6)	N00D	C00N	N009	114(2)
O006	Er01	N00B[3]	84.9(6)	N00G	C00O	N00D	116(2)
O007[1]	Er01	O003	118.3(5)	O007	C00P	C00J	129(2)
O007[1]	Er01	N00B[3]	125.5(6)	O007	C00P	C00M[1]	114(2)
O00A[2]	Er01	O003	143.9(5)	C00J	C00P	C00M[1]	117(2)
O00A[2]	Er01	O007[1]	66.4(5)	C00X	N00Q	C00T	99(2)
O00A[2]	Er01	N00B[3]	134.3(6)	O00A	C00R	C00I	125(2)
C00S	O002	Er01	124.4(14)	O00A	C00R	C00U[2]	113.7(19)
C00K	O003	Er01	116.6(13)	C00I	C00R	C00U[2]	121(2)
C00M	O004	Er01	121.2(14)	O002	C00S	C00K	110.0(19)
C00U	O005	Er01	120.2(16)	O002	C00S	C00W	130(2)
C00P	O007	Er01[1]	121.0(14)	C00W	C00S	C00K	119.6(17)
C00F	N008	C00J	121.7(19)	N00E	C00T	N00Q	113(2)
N00H	N008	C00F	112.3(19)	O005	C00U	C00I	123(2)
N00H	N008	C00J	126(2)	O005	C00U	C00R[2]	115(2)
C00I	N009	N00G	120.3(19)	C00I	C00U	C00R[2]	121.5(19)
C00N	N009	N00G	107.0(19)	N00H	C00V	N00B	113(2)
C00N	N009	C00I	132.5(19)	N00E	C00W	C00K[4]	119(2)
C00R	O00A	Er01[2]	116.0(15)	C00S	C00W	N00E	118.3(19)
C00F	N00B	Er01[3]	123.5(17)	C00S	C00W	C00K[4]	122(2)
C00F	N00B	C00V	105(2)	N00L	C00X	N00Q	118(2)

Table S9. Continuous SHAPE measurement (CShM) values of the 13 possible coordination geometries for the Er^{III} ion with coordination number 9 in **1a** and **1b**.[7]

	1a	**1b**
EP-9	35.360	37.136
OPY-9	23.761	21.660
HBPY-9	19.013	19.640
JTC-9	15.518	15.966
JCCU-9	10.426	10.461
CCU-9	9.140	9.497
JCSAPR-9	1.676	1.672
CSAPR-9	0.565	0.976
JTCTPR-9	2.191	1.653
TCTPR-9	0.979	0.532
JTDIC-9	13.722	12.866
HH-9	11.792	11.302
MFF-9	0.590	1.384

EP-9 = Enneagon; OPY-9 = Octagonal pyramid; HBPY-9 = Heptagonal bipyramid; JTC-9 = Johnson triangular cupola J3; JCCU-9 = Capped cube J8; CCU-9 = Spherical-relaxed capped cube; JCSAPR-9 = Capped square antiprism J10; CSAPR-9 = Spherical capped square antiprism; JTCTPR-9 = Tricapped trigonal prism J51; TCTPR-9 = Spherical tricapped trigonal prism; JTDIC-9 = Tridiminished icosahedron J63; HH-9 = Hula-hoop; MFF-9 = Muffin

Table S10. Continuous SHAPE measurement (CShM) values of the 13 possible coordination geometries for the Er^{III} ion with coordination number 8 in **1a_des**.[7]

OP-8	30.477
HPY-8	23.286
HBPY-8	15.656
CU-8	12.267
SAPR-8	4.494
TDD-8	1.887
JGBF-8	12.433
JETBPY-8	25.772
JBTPR-8	2.803
BTPR-8	2.103
JSD-8	3.334
TT-8	12.666
ETBPY-8	22.346

OP-8 = Octagon; HPY-8 = Heptagonal pyramid; HBPY-8 = Hexagonal bipyramid; CU-8 = Cube; SAPR-8 = Square antiprism; TDD-8 = Triangular dodecahedron; JGBF-8 = Johnson gyrobifastigium J26; JETBPY-8 = Johnson elongated triangular bipyramid J14; JBTPR-8 = Biaugmented trigonal prism J50; BTPR-8 = Biaugmented trigonal prism; JSD-8 = Snub diphenoid J84; TT-8 = Triakis tetrahedron; ETBPY-8 = Elongated trigonal bipyramid.

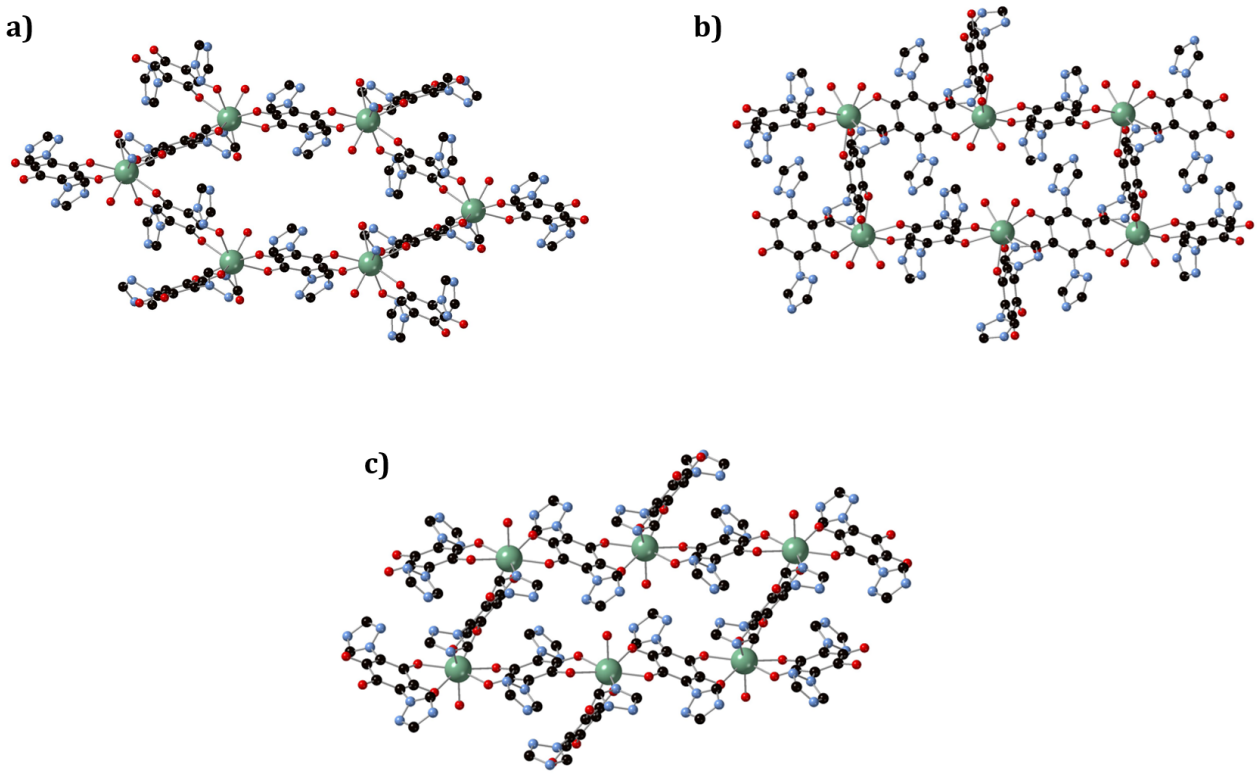

Figure S2. View of (a) one hexagonal cavitiy of **1a**, (b) one rectangular cavity of **1b** and (c) one shrinked rectangular cavity of **1a_des.**

Powder X-Ray Diffraction (PXRD)

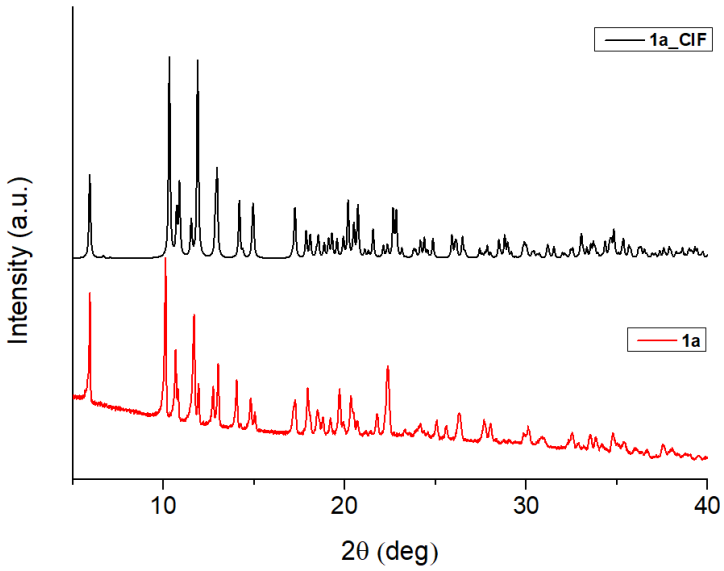

Figure S3. Experimental powder XRD pattern (red) and calculated pattern (black) of compound **1a**, in 2θ range of 5-40°.

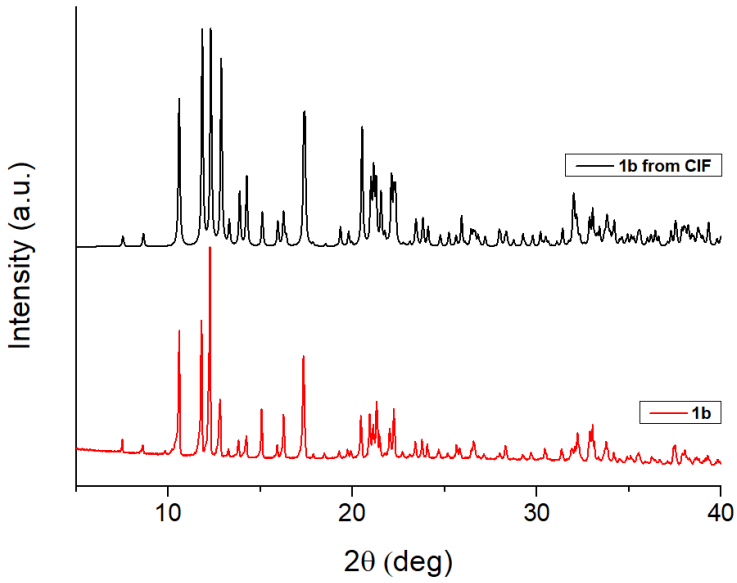

Figure S4. Experimental powder XRD pattern (red) and calculated pattern (black) of compound **1b**, in 2θ range of 5-40°.

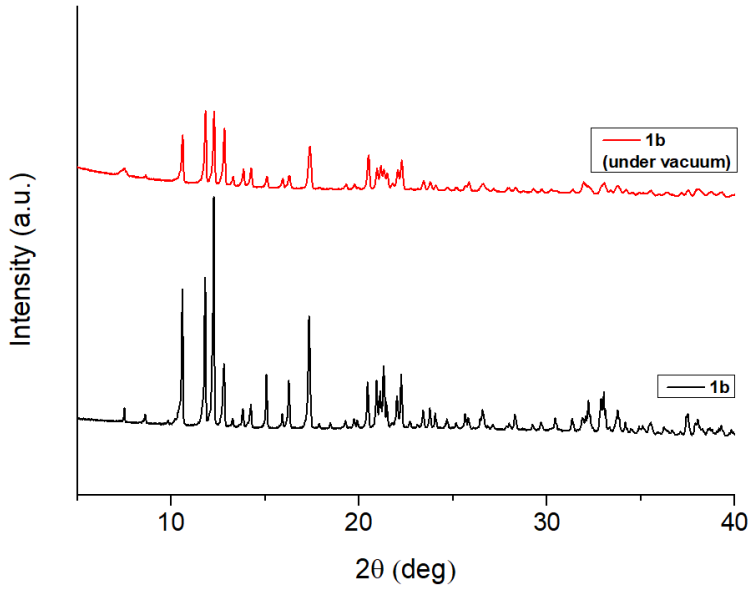

Figure S5. PXRD patterns of **1b** (black) and **1b** under vacuum (red) in 2θ range of 5-40°.

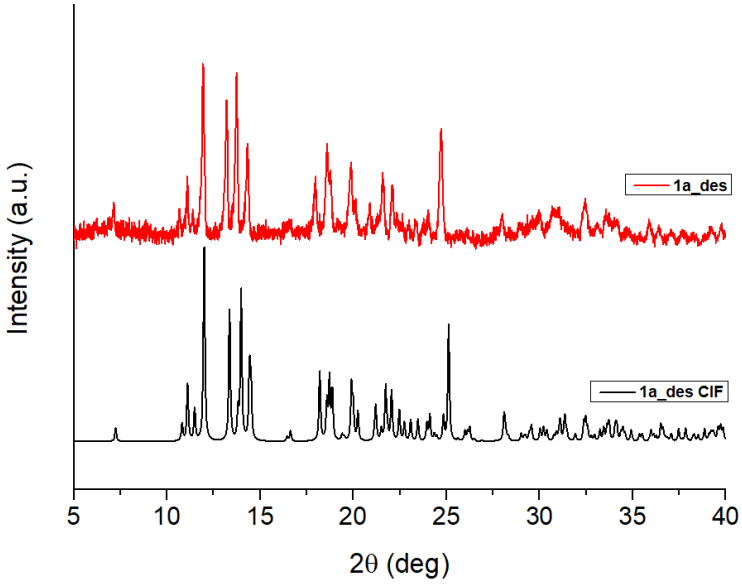

Figure S6. Calculated (black) and experimental (red) PXRD patterns of **1a_des**, in 2θ range of 5-40°.

3. FT-IR Spectroscopy

FT-IR spectra were collected using a Bruker Equinox 55 spectrometer, preparing the samples as KBr pellets.

The spectra of **1a** and **1b** were compared with H_2trz_2An spectrum. As shown in figure S1, the band at 1650 cm^{-1} of νCO of free ligand disappears and the broad band in the region around 1550 cm^{-1} is downshifted, due to the coordination of C-O in the frameworks.

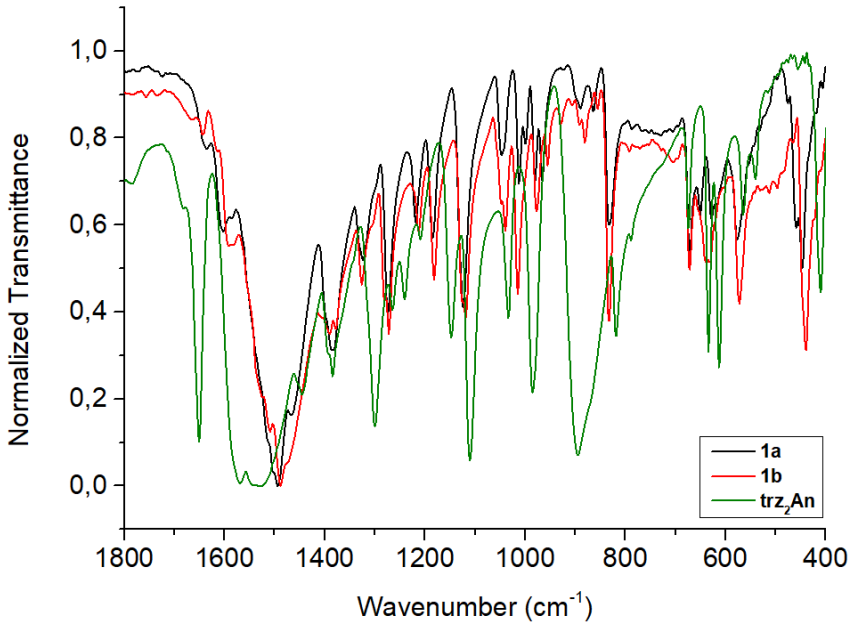

Figure S7. FT-IR spectra of H_2trz_2An (green), **1a** (black) and **1b** (red) in the 1800-400 cm^{-1} region.

FT-IR spectra of **1a** and **1b** appear very similar and show only slight differences in the bands. The characteristic bands with their assignments are shown in the following table.

Table S11. Assignments of characteristic bands for compounds **1a** and **1b**, all the frequencies are in cm^{-1}.[8–11]

	1a	**1b**
ν O-H	3388	3438
ν C=O	1605	1589
ν C=O + ν C=C aromatic	1513 1492	1506 1488
ν aromatic ring	1385	1391 1377
ν C-N	1321 1272	1325 1278 1272
ν N-N	1183	1181
δ C=C	835	835
ν Er-O	459 446	438

4. Thermogravimetric Analysis

Thermogravimetric analysis (TGA) was performed in order to study the thermal stability of both **1a** and **1b** and to have complementary information about the dehydrated phase **1a_des**. Thus, the first weight loss of 10 % from room temperature to 350 K is consistent with the change of chemical formula from $[Er_2(trz_2An)_3(H_2O)_4]_n \cdot 10H_2O$ found in **1a** by elemental analysis to $[Er_2(trz_2An)_3(H_2O)_2]_n \cdot 2H_2O$ found in the structure of **1a_des**. It was not possible to use elemental analysis to obtain the formula of this compound due to the fast rehydration of **1a_des** in air.

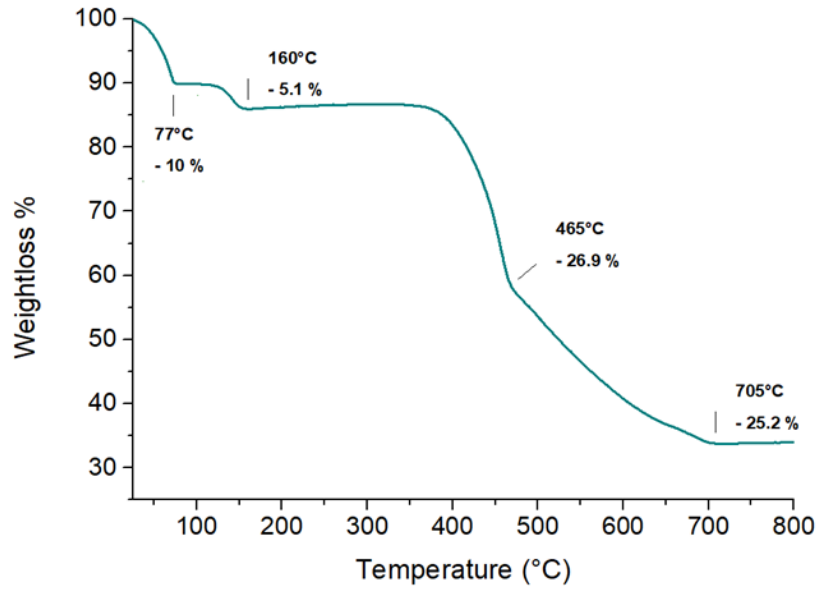

Figure S8. Thermogram of **1a** in 25-800°C temperature range. The percentages shown in the graph are referred to the previous weight loss.

1a thermogram shows a continuous weight loss of 10 % from room temperature to 77°C, which is close to the expected weight loss of 10 water molecules. Then in the 77-160°C temperature range a second weight loss is present, which is close to the expected weight loss for the remaining 2 solvate water molecules, leading to the formula $[Er_2(trz_2An)_3(H_2O)_2]_n$. Therefore, the first weigh loss in the 25-77°C corresponds to half of the coordinating water molecules and part of the solvate water molecules, while the one 77-160°C it could be due to the remaining solvate water molecules. Taking into account the crystallographic data, the first weight loss is consistent with the transition from the initial compound ($[Er_2(trz_2An)_3(H_2O)_4]_n \cdot 10H_2O$) to $[Er_2(trz_2An)_3(H_2O)_2]_n \cdot 2H_2O$ of **1a_des**. Then the second weight loss is close to the expected loss which lead to the formula $[Er_2(trz_2An)_3(H_2O)_2]_n$.

Thermogram of **1b**, reported in **Figure S8**, shows the first weight loss of 7.3% at 165°C, which correspond to 5.5 water molecules. At 213°C there is another weight loss of 2.7%, corresponding to 1.5 water molecules. As **1a**, the compound is very stable, starting its decomposition above 400°C, after the ligand decomposition.

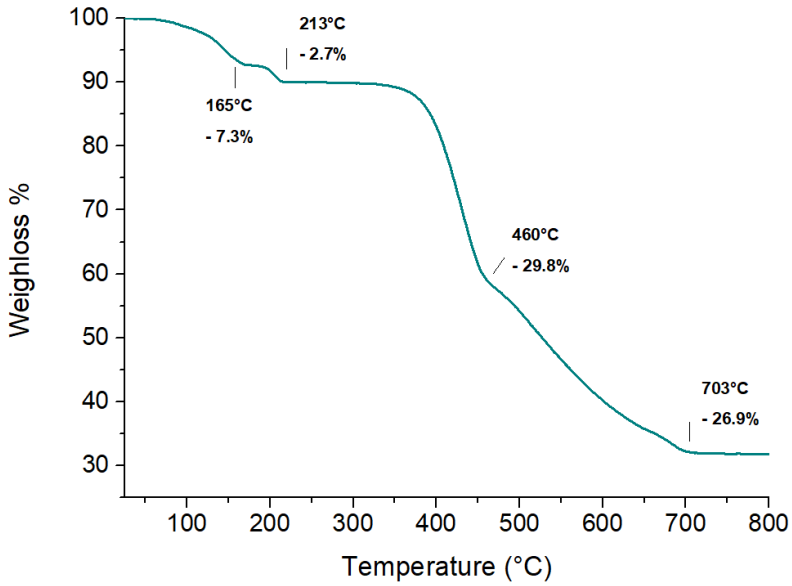

Figure S9. Thermogram of **1b** in 25-800°C temperature range, showing the weightlosses at different temperatures. The percentages shown in the graph refer to the previous one weightloss.

5. Magnetic Measurements

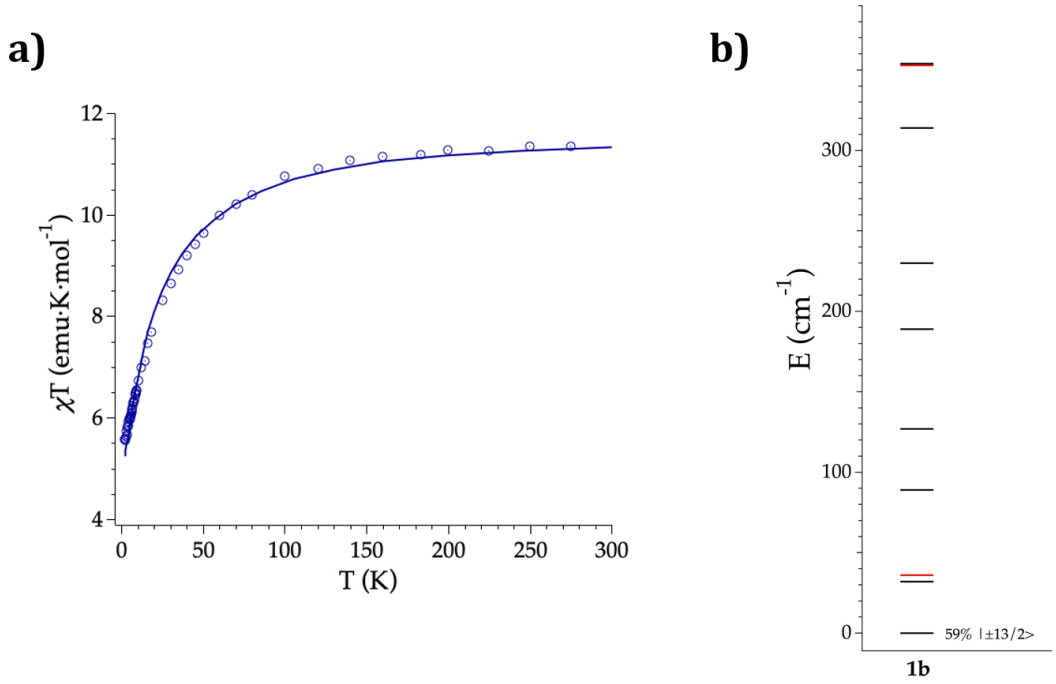

Figure S10. Experimental (symbols), fitted (solid line) temperature-dependence of the magnetic susceptibility from 2 to 300 K of **1b** (a); Calculated (black) and experimental (red) ground-*J* multiplet energy levels (b). Further details are provided in **Table S12**.

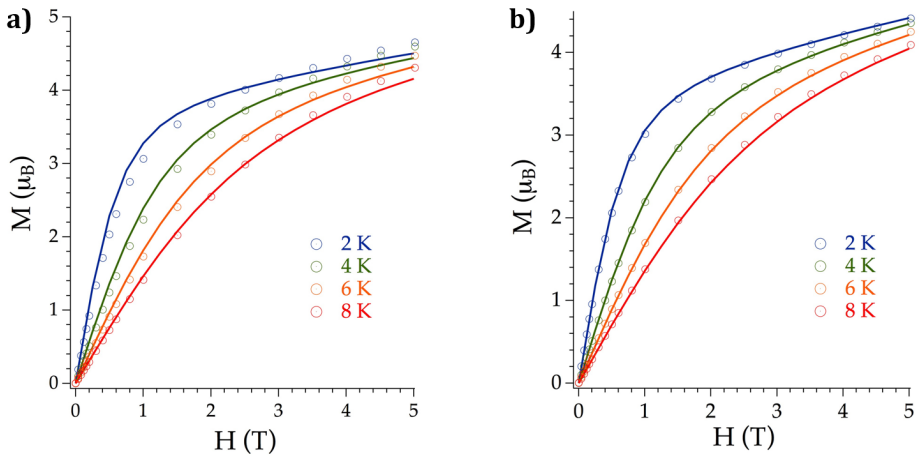

Figure S11. Experimental (symbols) and predicted average (lines) of magnetization M versus field H for **1a** (a) and **1a_des** (b) at 2K (blue), 4 K (green), 6 K (orange) and 8 K (red).

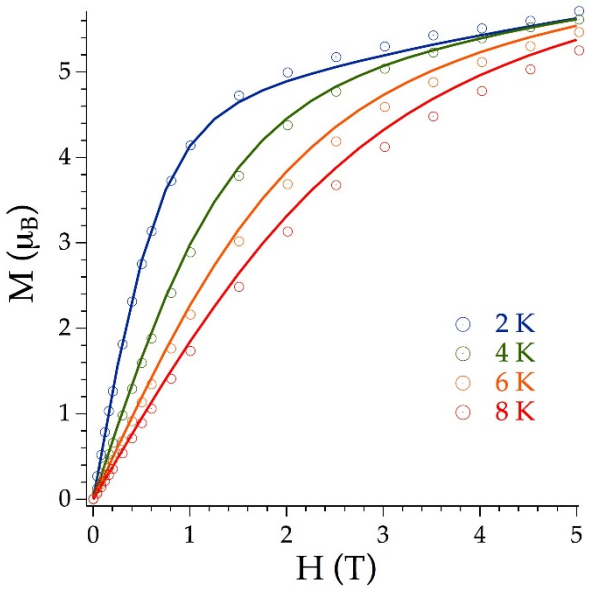

Figure S12. Experimental (symbols) and predicted average (lines) of magnetization M versus field H for **1b** at 2K (blue), 4 K (green), 6 K (orange) and 8 K (red).

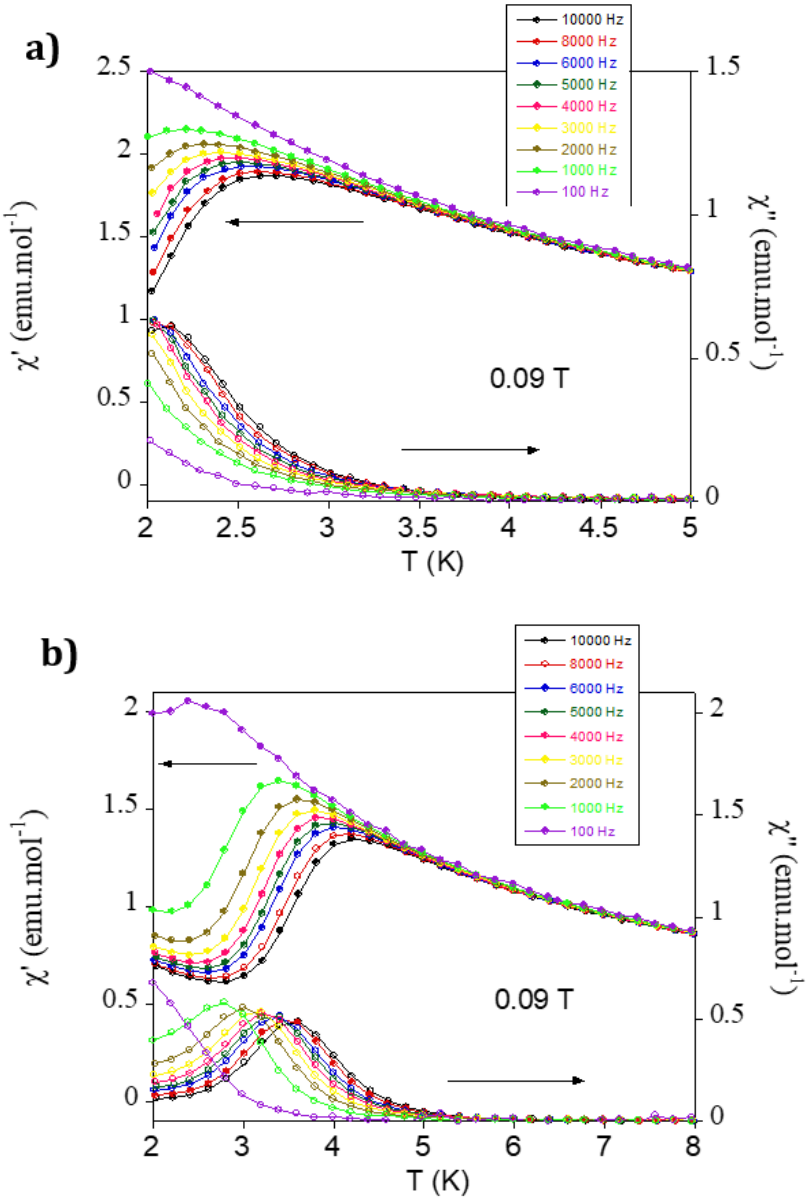

Figure S13. Temperature dependence of χ' and χ'' of **1a** (a) and **1a_des** (b) in an applied dc field of 0.09 T at frequencies in the range 100 to 10000 Hz.

a)

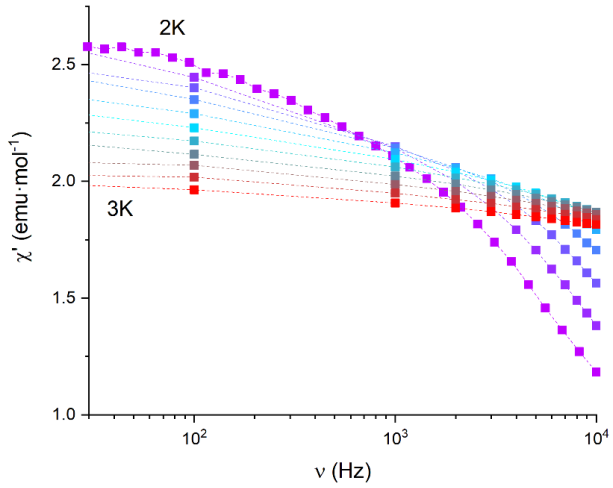

b)

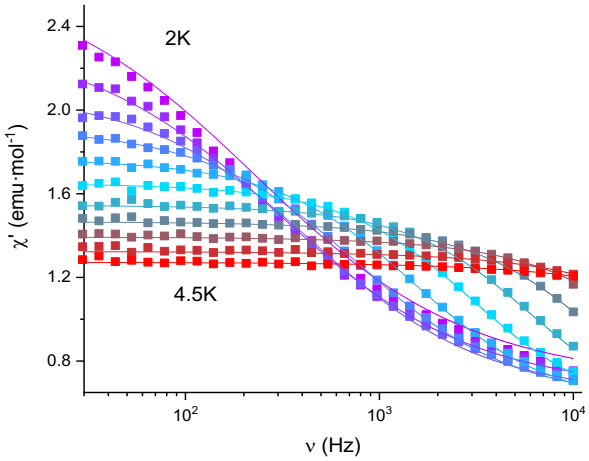

Figure S14. Frequency dependence of the in-of-phase component, χ', in an applied dc field of 0.09 T of **1a** (a) and **1a_des** (b) at different temperatures. Solid lines in **1a_des** represent the best fitting of the experimental data to a Debye function.

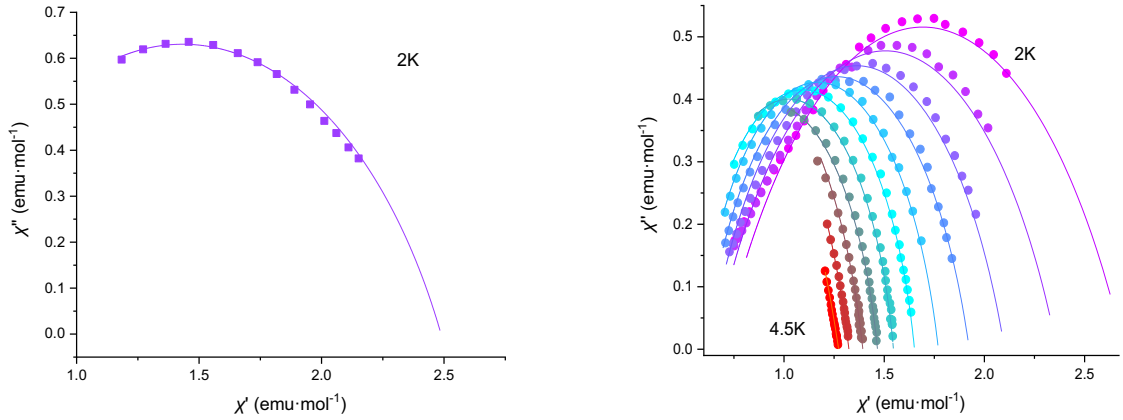

Figure S15. Cole-Cole plots of **1a** (left) and **1a_des** (right). Solid lines represent the best fitting of the experimental data to a Debye function.

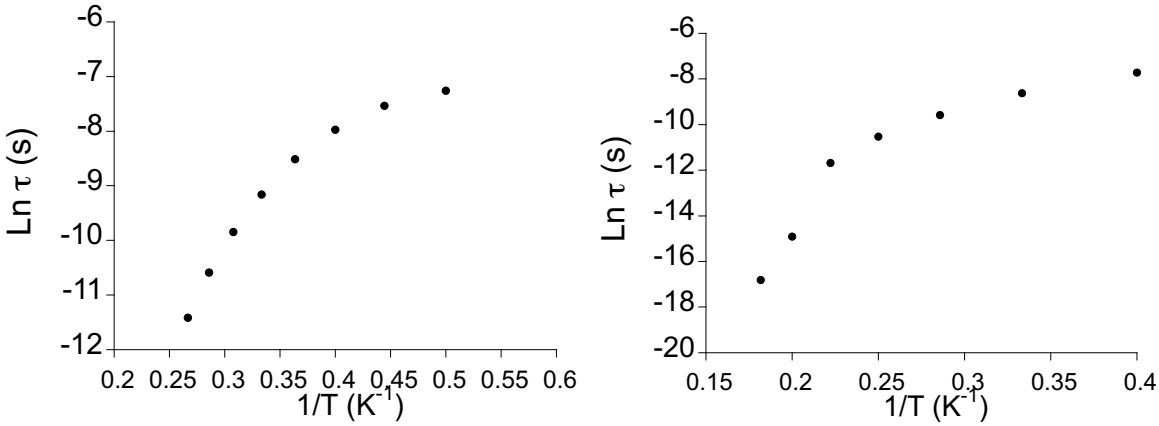

Figure S16. Plot of Ln τ versus T^{-1} for **1a_des** (left) and **1b** (right).

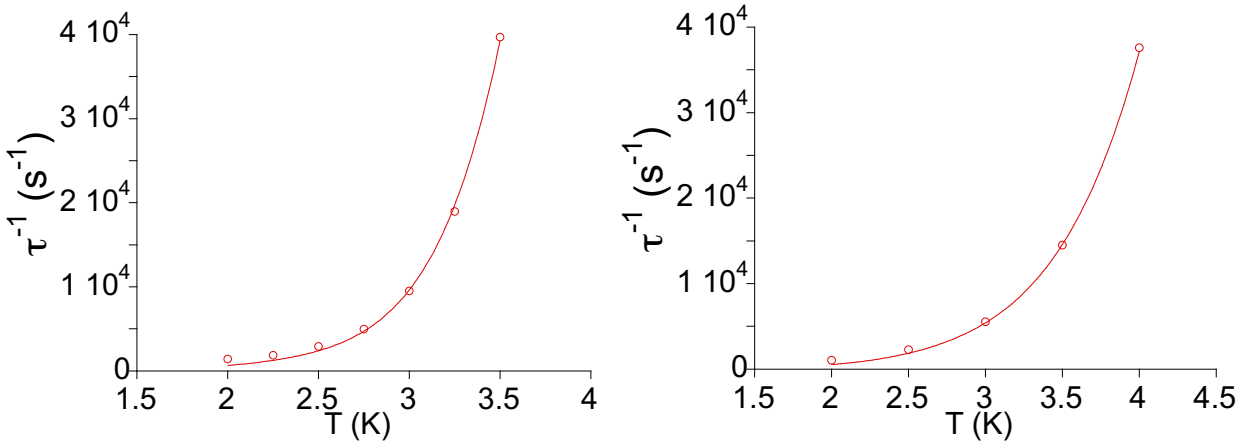

Figure S17. Thermal dependence of the relaxation time of **1a_des** (left) and **1b** (right) and best fit from two terms mechanism described in text.

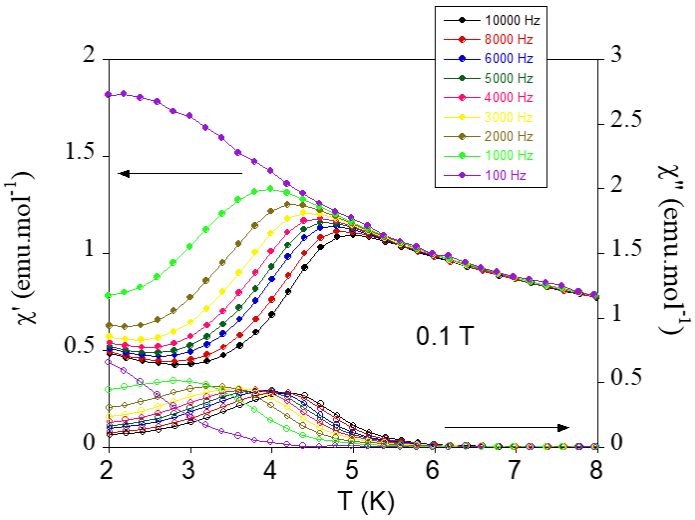

Figure S18. Temperature dependence of χ' and χ" of **1b** in an applied dc field of 0.1 T at frequencies in the range 100 to 10000 Hz.

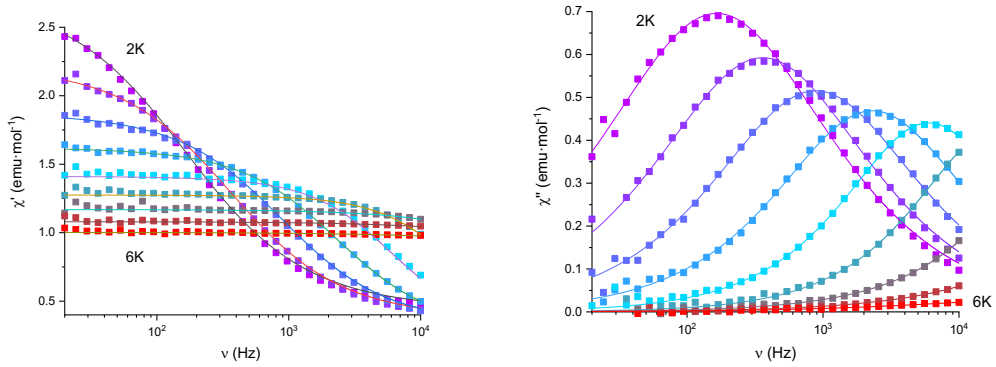

Figure S19. ac susceptibility in an applied dc field of 0.1 T of **1b** measured as a function of the frequency at the different temperatures (2.0, 2.5, 3.0, 3.5, 4.0, 4.5, 5.0, 5.5 and 6.0 K). Left: Real component. Right: Imaginary component. Solid lines represent the best fitting of the experimental data to a Cole-Cole function.

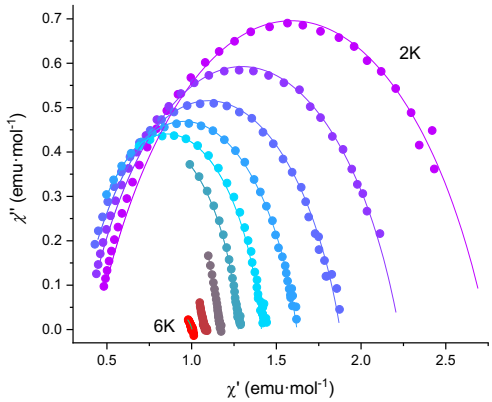

Figure S20. Cole-Cole plots of **1b** under an applied dc field of 0.1 T. Solid lines represent the best fitting of the experimental data to a Debye function.

6. Theoretical Calculations

Radial Effective Charge (REC) model

Our calculations start with the crystallographic/non-idealized atomic coordinates of the first coordination sphere. These are introduced as an input for the portable *fortran77* software code SIMPRE.[2] This code parameterizes the electric field effect produced by the surrounding ligands, acting over the central ion, by using the following Crystal Field Hamiltonian expressed in terms of the Extended Stevens Operators (ESOs):[12,13]

$$\hat{H}_{cf}(J) = \sum_{k=2,4,6} \sum_{q=-k}^{k} B_k^q O_k^q = \sum_{k=2,4,6} \sum_{q=-k}^{k} a_k (1-\sigma_k) A_k^q \left\langle r^k \right\rangle O_k^q \tag{1}$$

where k is the order (also called rank or degree) and q is the operator range, that varies between k and $-k$, of the Stevens operator equivalents O_k^q as defined by Ryabov in terms of the angular momentum operators $J_{\pm}$ and J_z,[14] where the components $O_k^{q(c)}$ and $O_k^{q(s)}$ correspond to the ESOs with q ≥ 0 and q < 0 respectively.[14] Note that all the Stevens CF parameters B_k^q are real, whereas the matrix elements of O_k^q (q < O) are imaginary. a_k are the α, β and γ Stevens coefficients[15] for k = 2, 4, 6, respectively, which are tabulated and depend on the number of f electrons. σ_k are the Sternheimer shielding parameters[16] of the 4f electronic shell, and $\langle r^k \rangle$ are the expectation values of the radius.[16]

In SIMPRE, the A_k^q CF parameters are determined by the following relations:

$$A_k^0 = \frac{4\pi}{2k+1} \sum_{i=1}^{N} \frac{Z_i e^2}{R_i^{k+1}} Z_{k0}(\theta_i, \varphi_i) p_{kq} \tag{2.a}$$

$$A_k^q = \frac{4\pi}{2k+1} \sum_{i=1}^{N} \frac{Z_i e^2}{R_i^{k+1}} Z_{kq}^c(\theta_i, \varphi_i) p_{kq} \tag{2.b}$$

$$A_k^q = \frac{4\pi}{2k+1} \sum_{i=1}^{N} \frac{Z_i e^2}{R_i^{k+1}} Z_{k|q|}^s(\theta_i, \varphi_i) p_{k|q|} \tag{2.c}$$

In the REC model[3] the ligand is modeled through an effective point charge situated between the lanthanoid and the coordinated atom at a distance R_i from the magnetic centre, which is smaller than the real metal-ligand distance (r_i). To account for the effect of covalent electron sharing, a radial displacement vector ($\mathbf{D_r}$) is defined, in which the polar coordinate r of each coordinated atom is varied, $R_i = r_i - D_r$. The usual procedure is to obtain the D_r parameter of each kind of donor

atom from a collective fit of an observable (e.g. energy levels or magnetic properties) for a family of isostructural lanthanide complexes. At the same time, the charge value (Z_i) is scanned in order to achieve the minimum deviation between calculated and experimental data, whereas θ_i and φ_i remain constant. In this work, we have kept fixed the value of D_r for the oxygen and nitrogen atoms, 0.98 Å and 1.20 Å, which have been taken from the literature (Chem. Sci., Inorg. Chem.) and offer a better approximation for the relative relation between k = 2, 4, 6, which is one of the main drawbacks of the point-charge electrostatic model. This strategy allows us to restrict the number of free parameters to 2, i.e. the effective charges of the nitrogen and oxygen atoms, *Zi* (N) = 0.05 and *Zi* (O) = 0.161, which have been obtained by a two-parameter fit of the χT product of both phases. Here it is worth to mention that these phenomenological parameters used by SIMPRE to predict the spin energy levels and wave functions do not pretend to simulate the actual charge distribution. In the fitting procedures, we define the relative error *E* as:

$$E = \frac{1}{n}\sum_{i=1}^{n}\frac{\left[\chi_{theo,i} - \chi_{\exp,i}\right]^2}{\left[\chi_{\exp,i}\right]^2} \tag{4}$$

where χ_{exp} and χ_{theo} are experimental and theoretical magnetic susceptibility, respectively, and n is the number of points.

To calculate the magnetic properties, SIMPRE introduces the interaction between the electron spin and an external magnetic field along the z-direction via a Zeeman term $\widehat{H}_{ZEE}$:

$$\widehat{H}_{ZEE} = g_j \mu_B B_z \cdot \hat{J}_z$$

Where g_j is the Landé *g*-factor for the ground *J*-multiplet, μ_B is the Bohr magneton, B_z is the external magnetic field along the z-direction and $\hat{J}_z$ is the z-component of the total electronic angular momentum operator. Once we have the eigenvalues of the system at different magnetic fields or temperatures, one can evaluate the partition function Z:

$$Z = \sum\nolimits_n \exp\left(-\frac{E_n}{kT}\right)$$

where E_n are the eigenvalues of the system, T is temperature and k is the Boltzmann constant. Then, the macroscopic thermodynamic properties, such as magnetization and magnetic susceptibility, are calculated by summing the N microscopic magnetizations weighed by according

to the Boltzmann distribution law, via the following fundamental equations:

$$M = NkT\frac{\partial lnZ}{\partial H}$$

Table S12. Crystal field parameters ($A_k^q < r^k >$; Stevens notation) in cm^{-1} obtained for **1a**, **1a_des** and **1b**.

k	***q***	**1a**	**1a_des**	**1b**
2	0	-109.47	-4.31	-235.64
2	1	536.28	-174.55	-23.17
2	-1	132.52	97.96	175.22
2	2	-9.96	443.83	-232.21
2	-2	1.21	156.58	47.37
4	0	53.25	177.50	-23.76
4	1	133.83	256.23	58.08
4	-1	126.58	58.57	411.70
4	2	280.14	-351.37	-287.91
4	-2	54.85	319.13	55.10
4	3	260.99	378.95	118.07
4	-3	218.69	36.18	90.32
4	4	-215.45	-114.76	-443.98
4	-4	35.80	302.00	224.24
6	0	19.33	-16.06	24.75
6	1	112.26	116.46	-18.66
6	-1	17.69	18.09	41.02
6	2	1.40	57.54	-81.76
6	-2	10.26	41.34	93.90
6	3	-266.50	-39.74	17.48
6	-3	121.33	292.07	77.70
6	4	-232.96	2.04	111.02
6	-4	103.40	44.61	145.96

6		732.41	-346.65	-623.85
6	5 - 5	249.20	431.47	65.11
6		167.56	16.77	123.27
6	6 - 6	193.08	10.26	225.20

Table S13. Ground multiplet energy level scheme (Kramers doublets in cm^{-1}) and main $|M_J>$ contributions to the wave function calculated for **1a** and **1a_des**. Red numbers in brackets: Main energy values estimated from PL spectrum of **1a_des** at 77K, assuming a zero-phonon transition wavelength of 1529 nm.

1a		**1a_des**	
0	59.5% |±13/2> + 14.7% |±5/2>	**0**	63.7% |±9/2> + 13.5% |±11/2> + 10.8% |±7/2>
39	36.6%|±11/2> + 14.0% |±3/2> + 16.3% |±1/2>	**42 (29)**	42.3% |±7/2> + 13.0% |±9/2> + 12.9% |±13/2> + 12.9% |±11/2>
94	17.4% |±11/2> + 20.6% |±7/2>	**73**	53.8% |±11/2> + 11.1% |±7/2>
158	10.6% |±11/2> + 12.8% |±9/2> + 12.1% |±7/2> + 12.2% |±3/2> + 13.1% |∓9/2>	**135**	49.4% |±5/2>
236	12.2% |±13/2> + 14.4% |±9/2> + 16.7% |±3/2> + 23.3% |±1/2>	**188**	44.8% |±13/2> + 14.5% |±3/2>
263	30.0% |±15/2> + 15.1% |±9/2> + 16.9% |±5/2>	**248**	31.9% |±3/2> + 22.7% |±13/2>
312	17.2% |±7/2> + 12.3% |±3/2> + 10.7% |±1/2> + 12.3% |∓3/2>	**312**	79.4% |±15/2>
350	22.0% |±15/2> + 26.8% |±7/2> + 11.2% |±5/2>	**390 (349)**	37.8% |±1/2> + 22.8% |∓1/2> + 18.6% |∓3/2>

Table S14. Ground multiplet energy level scheme (Kramers doublets in cm^{-1}) and main $|M_J>$ contributions to the wave function calculated for **1b**. Red numbers in brackets: Main energy values estimated from the PL spectrum of **1b** at 77K, assuming a zero-phonon transition wavelength of 1524 nm.

1b	
0	59.2% |±13/2>
32 (36)	33.4% |±11/2> + 29.7%|±15/2> + 12.3% |∓13/2> + 10.4% |∓1/2>
89	16.9% |±5/2> + 16.4%|±3/2> + 13.1% |∓3/2> + 11.6% |±1/2>
127	22.5% |±15/2> + 19.7% |±0.50> + 17.4% |∓3/2> + 13.4% |∓1/2>

189	22.0% |±11/2> + 16.7% |±9/2> + 12.0% |±5/2> + 11.6% |±7/2> + 11.3% |±15/2>
230	22.3% |±9/2> + 10.8% |±7/2> + 12.2% |∓15/2>
314	24.8% |±9/2> + 12.0% |∓7/2> + 10.7% |∓5/2> + 10.6% |±3/2>
354 **(353)**	33.6% |±7/2> + 27.8% |∓5/2> + 10.2% |±3/2>

7. Photoluminescence Measurements

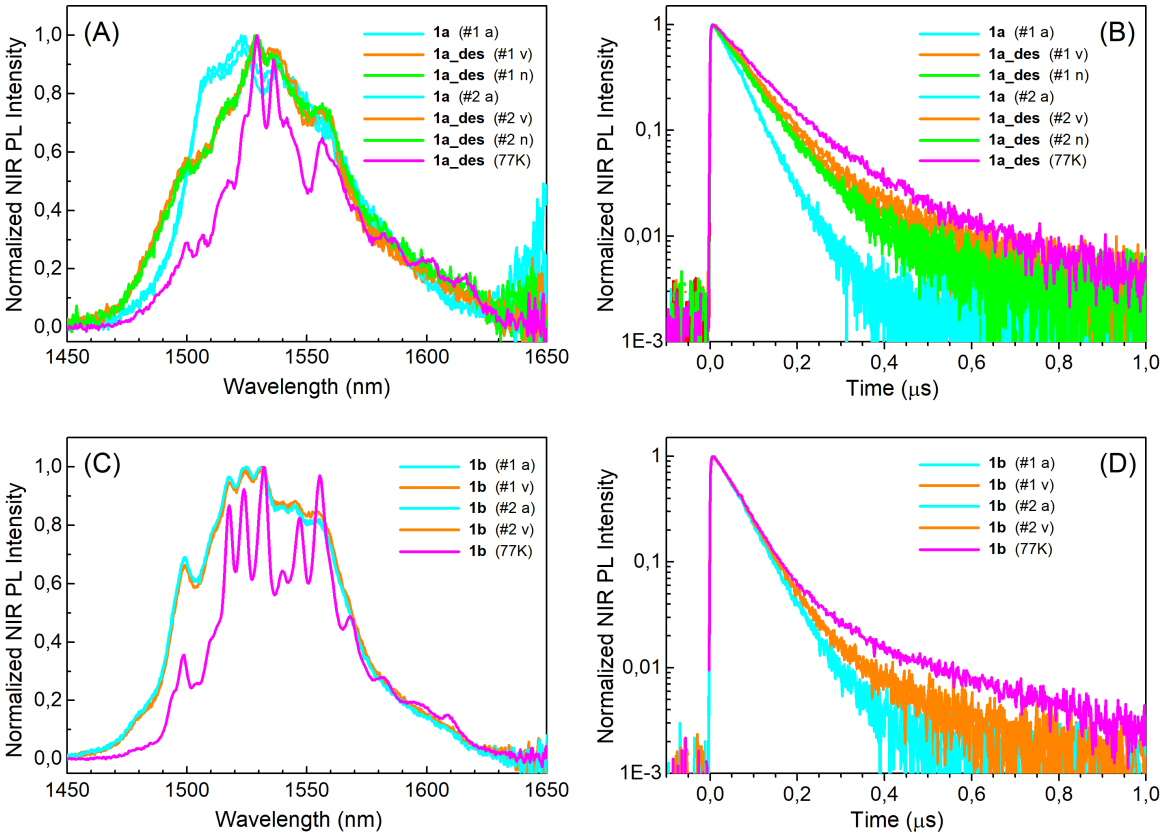

Figure S21. Demonstration of reversible Er^{III}-centred NIR PL properties in hydration/dehydration cycles. #1(2): First(second) measurement in air (a), under vacuum (v) and N_2 atmosphere (n). (A) NIR PL spectra of phase **1a** (in air) and **1a_des** (under vacuum and N_2). (B) NIR PL decay transients. (C,D) Same as (A,B) but for **1b**. All spectra and decay transient are normalized to their peak values for better clarity. Absolute PL intensities were reproduced within 5-10% after each cycle. At room temperature, all phases displayed the same integrated PL intensity within 10%. Cooling to 77K produced less than a factor of two increase in integrated PL intensity in both **1a_des** and **1b**.

8. References

1 W. Gauβ, H. Heitzer and S. Petersen, *Justus Liebigs Ann. Chem.*, 1973, **764**, 131–144.

2 J. J. Baldoví, S. Cardona-Serra, J. M. Clemente-Juan, E. Coronado, A. Gaita-Ariño and A. Palii, *J. Comput. Chem.*, 2013, **34**, 1961–1967.

3 J. J. Baldoví, J. J. Borrás-Almenar, J. M. Clemente-Juan, E. Coronado and A. Gaita-Ariño, *Dalt. Trans.*, 2012, **41**, 13705–13710.

4 G. M. Sheldrick, *Acta Crystallogr. Sect. A Found. Crystallogr.*, 2015, **71**, 3–8.

5 G. M. Sheldrick, *Acta Crystallogr. Sect. C Struct. Chem.*, 2015, **71**, 3–8.

6 O. V. Dolomanov, L. J. Bourhis, R. J. Gildea, J. A. K. Howard and H. Puschmann, *J. Appl. Crystallogr.*, 2009, **42**, 339–341.

7 M. Llunell, D. Casanova, J. Cirera, P. Alemany and S. Alvarez, *Univ. Barcelona Barcelona, Spain*.

8 F. M. A. Kerim, H. F. Aly and A. El-Agramy, *Proc. Indian Acad. Sci. - Sect. A*, 1977, **85**, 559–566.

9 M. K. Trivedi, R. M. Tallapragada, A. Branton, D. Trivedi, G. Nayak, R. K. Mishra and S. Jana, *J. Mol. Pharm. Org. Process Res.*, 2015, **03**, 1–6.

10 O. Roubeau, B. Agricole, R. Cle and S. Ravaine, *J. Phys. Chem. B*, 2004, **108**, 15110–15116.

11 Q. Deng, C. Tian, Z. Luo, Y. Zhou, B. Gou, H. Liu, Y. Ding and R. Yang, *Chem. Commun.*, 2020, **56**, 12234–12237.

12 C. Rudowicz, *J. Phys. C Solid State Phys.*, 1985, **18**, 3837.

13 C. Rudowicz and C. Y. Chung, *J. Phys. Condens. Matter*, 2004, **16**, 5825–5847.

14 I. D. Ryabov, *J. Magn. Reson.*, 1999, **140**, 141–145.

15 K. W. H. Stevens, *Proc. Phys. Soc. Sect. A*, 1952, **65**, 209–215.

16 S. Edvardsson and M. Klintenberg, *J. Alloys Compd.*, 1998, **275**–**277**, 230–233.